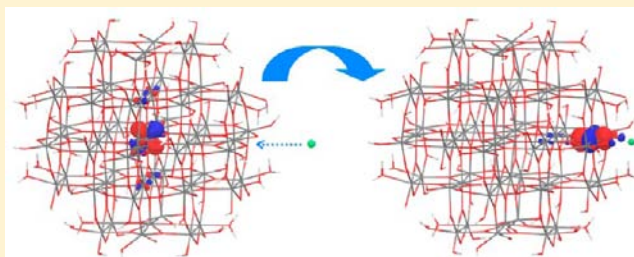# Realistic Cluster Modeling of Electron Transport and Trapping in Solvated TiO$_2$ Nanoparticles

Jing Zhang, Thomas F. Hughes, Michael Steigerwald, Louis Brus, and Richard A. Friesner*

Department of Chemistry, Columbia University, New York, New York 10027, United States

Ⓢ Supporting Information

ABSTRACT: We have developed a cluster model of a TiO$_2$ nanoparticle in the dye-sensitized solar cell and used first-principles quantum chemistry, coupled with a continuum solvation model, to compute structures and energetics of key electronic and structural intermediates and transition states. Our results suggest the existence of shallow surface trapping states induced by small cations and continuum solvent effect as well as the possibility of the existence of a surface band which is 0.3−0.5 eV below the conduction band edge. The results are in uniformly good agreement with experiment and establish the plausibility of an ambipolar model of electron diffusion in which small cations, such as Li$^+$, diffuse alongside the current carrying electrons in the device, stabilizing shallowing trapping states, facilitating diffusion from one of these states to another, in a fashion that is essential to the functioning of the cell.

1. INTRODUCTION

The dye-sensitized solar cell (DSSC) is one of the few novel solar energy conversion devices that is not based on silicon, yet is capable of relatively high conversion efficiencies of light to electricity while possessing low manufacturing costs. As such, it has stimulated a tremendous effort by the research community to better understand its functioning. Intensive experimental efforts have yielded a wealth of information with regard to various properties of the cell (e.g., carrier dynamics, electrochemistry, current/voltage characteristics, etc.), and a large number of variants in terms of dye molecules, electrolytes, redox couples, etc. have been investigated.[1−7]

From a phenomenological standpoint, much is now understood about what goes on in a functioning unit. The DSSC operates via a cascade of events involving a number of key components. Light is absorbed by dye molecules (typically ruthenium complexes) adsorbed to the surface of TiO$_2$ nanoparticles, which constitute the dominant constituent of the cell. The excited dye molecules inject an electron into the TiO$_2$ nanoparticle, where it rapidly is localized in a shallow trapping state from which the back reaction to the dye is a very low probability. The electron then proceeds via a thermally activated hopping mechanism to move through a dense TiO$_2$ nanoparticle network to the collection electrode. To complete the circuit, a redox couple (the I$_3^-$/I$^-$ couple is by far the most efficacious redox agent for the DSSC that has been found to date) in solution is employed; the reduced member of the couple donates an electron to replenish the dye molecule after it injects an electron into the TiO$_2$, while the oxidized member of the couple is reduced at the collection electrode, thus completing the circuit.

However, accurate microscopic models of structures and energetics, at an atomic level of detail, have been much more difficult to produce. Arguably, such models require reliable, high-quality theoretical calculations to complement experiments, which cannot obtain high-resolution structural data or the corresponding energies of many of the key participant electronic states, due to the complex, disordered nature of the system which is not amenable to standard techniques like X-ray diffraction analysis. While there have been many first-principles quantum chemical calculations of TiO$_2$ systems (some using periodic boundary conditions, others using cluster-based approaches),[8−14] these have suffered from a significant number of deficiencies with regard to relevance to DSSC functioning. We enumerate these deficiencies below and briefly describe what we have done in an attempt to remedy them:

(1) The great majority of calculations have been performed in vacuum, whereas the DSSC operates in a solution phase environment, which invariably contains a significant aqueous component. As we shall show below, immersion of the nanoparticles in a high-dielectric solvent (modeled as a dielectric continuum, which we believe to be a very good approximation for purposes of the present study) has a profound effect on structures and energetics, to the point where gas-phase results are unlikely to provide even a good first-order approximation to the correct physics or chemistry of the actual target system.

(2) It is generally assumed that the surface of the nanoparticles is passivated with water derived ligands.

(3) To our knowledge, there is no prior work in which such passivation has been imposed in a systematic fashion, aside from our earlier paper[15] on this subject. Use of a realistically passivated surface will emerge below as a critical component in building physically useful models.

(3) A major focus of computational work on TiO_2 is understanding what kind of structures and electronic states could lead to trapping of injected electrons; based on experimental data, such states are clearly central to carrier transport in the DSSC. Most prior computational work has focused on trapping states created by oxygen vacancies,[16−20] also see the latest reviews;[21,22] such states are no doubt significant for bulk TiO_2 in vacuum, but their relevance to transport in the DSSC is likely to be quite low, due to: (a) passivation of the surface with water derived ligands as noted in (2) above, which would potentially modify such vacancies drastically from the idealized models that are typically used in calculations; (b) these are generally deep traps (∼1 eV below the conduction band)[23] which may become filled with electrons; however, the states that actually participate in the thermally activated electron hopping process that describes transport in the DSSC must be much closer in energy to the conduction band, both because thermal activation would otherwise be precluded and also because a large separation between the dominant participating states and the conduction band would lead to a drastically lowered open circuit voltage and hence fail to capture much of the photon energy injected into the system. To the extent that these states exist in the actual environment, they will rapidly become filled from early electron injection; however, the states involved in subsequent carrier transport must be of a very different character.

(4) It has been clear for some time that the electrolyte in the cell, particularly the cations, plays a major role in carrier transport; in high-performing cells, the Li^+ cation is invariably used, and cell characteristics show significant dependence upon Li^+ concentration. These observations have led a number of groups to propose an ambipolar model for carrier transport,[24−29] in which small cations, such as Li^+, move with the migrating electrons, stabilizing shallow trapping states on or near the surface of the nanoparticle; such models have previously been suggested as being relevant to transport in other important electrical materials, such as batteries.[30−39] However, previous calculations aimed at the DSSC have not incorporated such ions in the model or investigated whether the ambipolar diffusion model is consistent with computational as well as experimental data. We perform initial work in these directions below, which yields highly encouraging results.

(5) The ability of DFT methods to compute experimentally relevant quantities for transition-metal-containing systems of the size and complexity of even a TiO_2 nanoparticle fragment in solution is far from clear. In a series of recent papers, we have shown that standard DFT methods make systematic errors for the calculation of quantities, such as redox potentials,[40] spin splitting energetics,[41] and average ligand removal enthalpies;[75] furthermore, we have developed an empirical model which provides robust and accurate corrections to these systematic errors. The model is based on a localized

orbital correction (LOC) scheme combined with the B3LYP functional[47] and yields, for example, a 0.1 eV mean unsigned error for redox potentials, a set of 95 octahedral transition-metal complexes. We employ this B3LYP-LOC methodology in the present paper and show that the calculation of key experimental quantities is dramatically improved with the LOC corrections, which are taken without any further modification from the values obtained in ref 40.

(6) The use of a surface passivated with water derived ligands, a continuum solvation model, a hybrid DFT functional, such as B3LYP, and explicit inclusion of net charge (excess electrons and cations) in the model system requires that a cluster modeling approach be employed. This in turn leads to very significant technical challenges, including treatment of a sufficiently large system, converging geometry optimization of this system in solvent for many structures, elimination of finite size effects when these interfere with important experimental comparisons, and the design of cluster models appropriate to the actual experimental systems. These problems have in general simply not been considered previous work and required a considerable effort to address in a satisfactory fashion. We only briefly summarize these efforts below, as we here wish to focus on the results rather than the mechanics of the calculations; a subsequent paper will present methodological advances in more detail.

In the present paper, we focus primarily upon modeling the TiO_2 nanoparticle (as opposed to other components of the DSSC, such as the adsorbed dye or redox couple) in an attempt to understand the structural and energetic parameters characterizing the trapping states involved in transport and to make an initial computational assessment of the plausibility of the ambipolar diffusion model. As noted above, our approach to these calculations differs from prior publications in the literature in many dimensions. A particular objective of this work is to establish extensive, quantitative linkages between the calculations and the important experimental observables. A believable theoretical model that is going to be useful to experimentalists in interpreting their data and in creating new, improved solar energy conversion systems must be validated by making as many points of contact with experiments, performed under ambient conditions (e.g., in solution rather than in vacuum), as is possible. Few such points of contact are manifested in previous work. In the present paper, we calculate, without any parameter fitting, properties, such as the position of the conduction band edge, open circuit voltage, trap depth, conduction band shift upon binding of Li^+, and barrier to ambipolar diffusion for a number of model geometries, and compare the results with available experimental data. The critical role of the localized orbital corrections is clear from this comparison. The results provide a solid basis for advancing the model further and ultimately drawing predictive conclusions, potentially of use for design purposes.

2. METHODOLOGY

2.1. DFT Calculations. As mentioned above, we previously modeled reduced TiO_2 nanoparticle in presence of continuum solvent[15] and employ a similar method in current work. Detailed aspects of the DFT calculations can be found in Supporting Information. All calculations in this work were
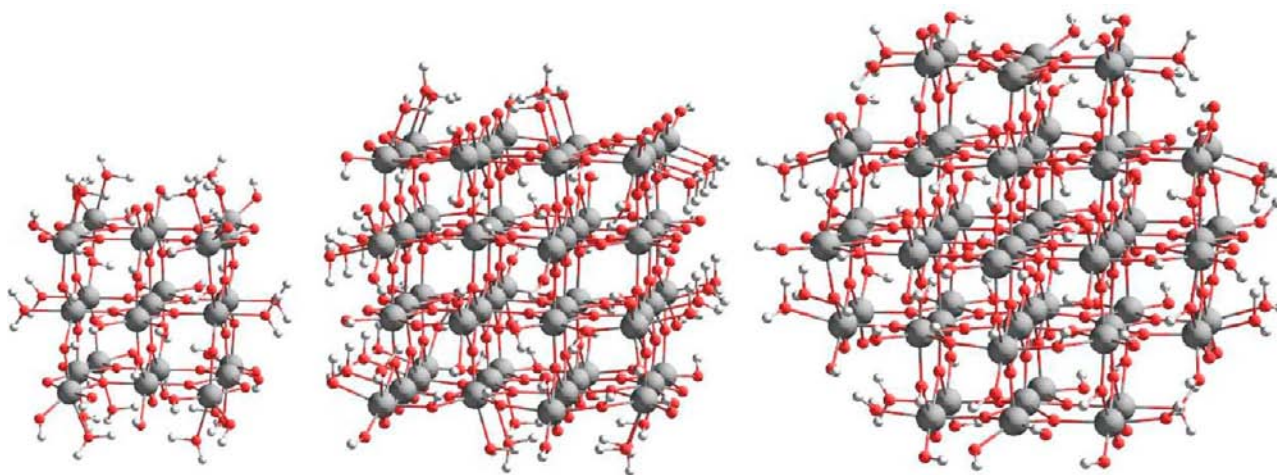
Figure 1. Model clusters, from left to right, are (3,3,3), (4,4,4), and (5,5,5) clusters. Titanium, oxygen and hydrogen atoms are shown in gray, red, and white, respectively.

performed at ROB3LYP/LACVP level using the DFT code Jaguar 7.7[42] with modified OpenMP/MPI hybrid parallel implementation on a 48-core workstation. Fully geometrical optimization was performed for all vacuum and continuum water calculations, and no symmetry and no geometric constraint (except explained in Supporting Information) is assumed; those calculations for continuum acetonitrile were single point calculations with the corresponding optimized geometry in continuum water. The continuum solvent effect was modeled by Poisson−Boltzmann continuum solvation method available in the Jaguar 7.7 code. The dielectric radii, which decide the reaction field, were chosen to be 1.600, 1.587, and 1.309 Å for O, Ti, and Li atoms, respectively. The value listed above for O and Ti atoms are default values in Jaguar, and the dielectric radius of the Li atom has been refitted to reproduce the experimental hydration enthalpy of the Li^+ cation.[43−46]

2.2. Calculation of Properties. The electric potential of the half reaction $O + ne^- \rightarrow R$ is calculated via

$$\varphi_{O/R} = -\frac{E(R) - E(O)}{n} - 4.44eV + \varphi_{loc} \qquad (1)$$

where $E(O)$ and $E(R)$ are the absolute energies of oxidized and reduced species from DFT calculations including the continuum solvation effect, 4.44 eV is the electric potential for the standard hydrogen reference electrode (SHE), and φ_{loc} is the localized orbital correction (explained below) for the redox potential error of transition-metal-containing species,[40] and this value for the TiO_2 cluster with the B3LYP functional is +0.48 eV. The use of the SHE as the reference potential is standard practice in the electrochemical literature.[67]

We provide here a brief description of the origin of the LOC correction parameters for redox potentials in the B3LYP-LOC methodology; details can be found in refs 40, 41, and 47−51. The LOC model was initially developed to correct reaction energies, ionization potentials, electron affinities, and barrier heights in DFT (and B3LYP in particular) for compounds composed of second- and third-row atoms. The basic idea is that the dominant errors in B3LYP involve an incorrect estimation of the nondynamical correlation energy in localized electron pairs (bond pairs, lone pairs) and that the error is dependent upon the local chemical environment of the electron pair in question (as in a valence bond approach), and hence a

correction term is transferable for that chemical environment from one molecule to the next. Average mean unsigned errors of 1 kcal/mol, i.e., near-chemical accuracy, have been obtained for large data sets for all of the quantities listed above. In recent work, we have extended the LOC model to transition-metal complexes, treating spin splittings, redox potentials, and metal−ligand dissociation energies, all of which exhibit large errors for a significant fraction of transition-metal-containing systems, when DFT approaches are employed. For purposes of this paper, the corrections for redox potentials are most relevant. We investigated a set of 95 octahedral complexes containing metals from first transition-metal series, with a variety of different ligands. Included in this data set were a number of titanium/oxygen compounds, with structures related to those seen in the TiO_2 clusters considered here. We found that the DFT-computed redox potentials were systematically shifted from experiment according to the chemical nature of the ligands, with a strong correlation between the observed errors and the positioning of the ligands in the spectrochemical series. A compact set of 7 parameters reduced the mean unsigned error in the redox potentials from ∼0.4 to 0.1 eV. We utilize the relevant parameters in the present paper to correct the redox potential of the TiO_2 cluster when an excess electron is added. In modeling the correction, we assume that the excess electron wave function is predominantly localized on a single titanium, an assumption that appears to be quite reasonable for all of the calculations discussed below. Given this assumption, application of the parameters from ref 40, which are used as is, is straightforward, as is displayed in eq 1 above. The parameters we use are dependent upon the oxo ligands and are not specialized to titanium; if we were to develop parameters specific for titanium complexes, the results would in fact be a little closer (∼0.1−0.2 eV) to experiment than those shown here. However, such a protocol has not been extensively tested, so we use the generic oxo parameters in what follows.

2.3. Model Clusters. The rutile TiO_2 nanoparticle was modeled using a water-passivated TiO_2 model cluster, which has real surfaces in all dimensions. The construction of our model clusters is based on four criteria: (1) The size of the cluster should be large enough to correctly produce the conduction and valence band structures; (2) the cluster should have enough atoms to represent the bulk, intermediate, and surface regions respectively; (3) the cluster, especially the

surfaces, should be stable under geometrical optimization; and (4) the cluster can be modeled with reasonable computational effort. We then constructed three TiO$_2$ model clusters shown in Figure 1 and named them as the (3,3,3), (4,4,4), and (5,5,5) model cluster based on the number of layers on each dimension. The procedure of cluster construction is described as follows: First, a cubic chunk of rutile TiO$_2$ crystal with four (110) and two (001) surfaces is cropped out from the crystal structure. Then if the cluster chunk is too big, several atoms at each corner are removed to constrain total number of atoms to be less than 400 but still maintain as many buried titanium atoms as possible. Finally the (110) surfaces are passivated with water molecules, and the (001) surfaces are capped by covalent O−H bonds. The basic properties of our model clusters are summarized in Table 1. Our (5,5,5) model cluster is

Table 1. Summary of Properties of TiO$_2$ Model Clusters

property	(3,3,3)	(4,4,4)	(5,5,5)
stoichiometry	Ti$_{23}$H$_{68}$O$_{80}$	Ti$_{56}$H$_{120}$O$_{172}$	Ti$_{61}$H$_{116}$O$_{180}$
symmetry	D_{2h}	C_{2h}	C_1
size (nm)	$0.9 \times 0.6 \times 0.7$	$1.1 \times 1.1 \times 0.9$	$1.5 \times 1.2 \times 1.2$
averaged radius (nm)	0.38	0.51	0.67
volume (nm^3)	0.4	1.0	1.0
number of buried Ti atoms	1	6	15

significantly larger than those used in prior studies. The stoichiometry of (5,5,5) cluster is Ti$_{61}$H$_{116}$O$_{180}$, the averaged "diameter" of the cluster is around 1.3 nm, and the volume is about 1.0 nm^3. There are 1, 14, and 46 Ti atoms representing bulk, intermediate, and surface regions, which provides both diverse surface and bulk interstitial sites. All studies below were carried out using the (5,5,5) model cluster. The (3,3,3) and (4,4,4) clusters were used primarily to facilitate the estimation of finite size effects and to calculate the finite size correction for continuum solvent effects as appropriate.

There are mainly two kinds of systems investigated in this article based upon the (5,5,5) TiO$_2$ model cluster. The first one is a pure TiO$_2$ cluster in continuum water; we first calculated the electronic structure of neutral and reduced (5,5,5) clusters in continuum water, then explored the finite size effect on the solvation energy of excess electron, and finally extrapolated out the band edge potentials for the actual TiO$_2$ nanoparticle. The second system is focused on TiO$_2$/Li; Li$^+$ is either adsorbed on the surface or intercalated into a first-shell interstitial site near

the surface, and both cases were investigated with regard to electron trap state, trap depth, conduction band movement, ambipolar diffusion barrier, open circuit voltage, and chemical reaction cycle. Finally, we summarize and compare our predicted properties to experimental results.

We employ a continuum solvation model (dielectric 80 for water, 37.5 for acetonitrile) to model bulk (as opposed to first shell) solvation effects in what follows. Both solvents possess a very high dielectric constant, which in fact is often approximated by a single model, the conductor-like screening model (COSMO),[52] which does not differentiate at all between two values of this magnitude. Arguments along the same lines can be inferred from a simple Born model of solvation (a charge in a spherical cavity surrounded by a medium of dielectric constant ε, in which case the solvation free energy is proportional to the term $1 - 1/\varepsilon$, in which case the difference in value when 37.5 or 80 is used is negligible. To the extent that there are differences between the two solvents, the use of the water dielectric model would be appropriate if multiple layers of aqueous solvent surround the TiO$_2$ nanoparticles, whereas the acetonitrile dielectric would represent a system in which the particles are passivated by a single layer of water derived ligands but then surrounded by acetonitrile solvent. As it is not clear which model better represents the actual situation in the DSSC, we explore both models in computing quantities most likely to be affected (discussed in more detail in the next paragraph). For other cases which we judge to be insensitive to the dielectric difference, such as the barrier height in our model ambipolar diffusion calculation, we employ dielectric 80.

We explore the effectiveness of aqueous solvation versus acetonitrile solvation in estimating the open circuit voltage of our model, a critical quantity in understanding the efficiency of the cell and in validating the computational model of relevant trapping states that we develop via comparison with experimental data. The redox potential of the I$_3^-$/I$^-$ couple in water vs acetonitrile is slightly different (~0.2 eV), possibly due to specific interactions of the solvent with the ions in the first solvation shell. As is shown below, the use of either solvent produces agreement with experiment that is within the likely errors of the computational models (0.1−0.2 eV). Finally, we have performed a number of other calculations in both water and acetonitrile, including the position of the conduction band edge in both solvents and the trap depth of a Ti^{3+} ion at the cluster surface stabilized via binding of a Li$^+$ cation. The numbers for water and acetonitrile are reported in Table 4. In general, deviations in the cluster model energy differences are
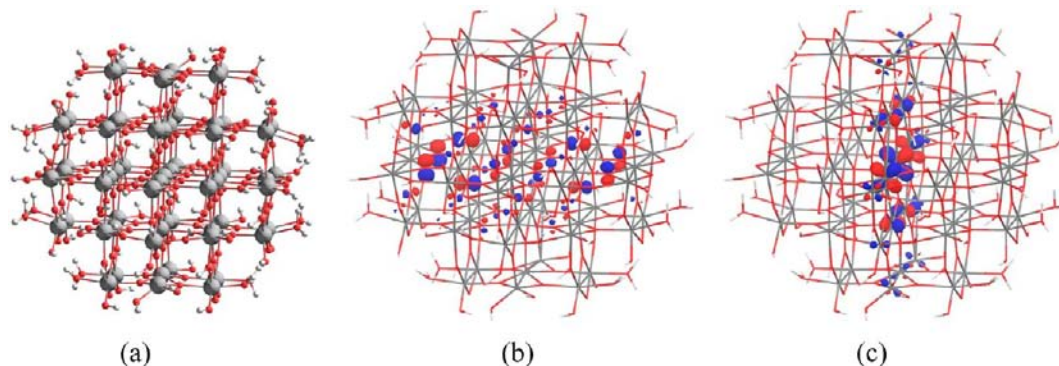

Figure 2. (a) Converged geometry of neutral TiO$_2$ cluster in continuum water. Titanium, oxygen, and hydrogen atoms are shown in gray, red, and white, respectively. (b) HOMO and (c) LUMO are shown in red and blue isocontour surfaces.

less than 0.05 eV, confirming the point made above that the difference in the results when one uses a dielectric constant of 80 as opposed to one of 37.5 are minimal.

In what follows, we at various points contrast results from performing calculations in continuum solvent to those obtained using the bare cluster. We refer to the bare cluster results as "vacuum" calculations, despite the fact that the cluster is in fact passivated with an entire layer of water derived ligands. This differs from some conventional uses of this term (particularly in the physics literature), but it is appropriate and convenient for the present work, as we make no attempt to produce a true "vacuum" cluster with no water adsorbed at all. In fact, exactly what such a cluster should look like is far from clear; the nature of the surface will depend upon the details of preparation of the material. In any case, such a state is not relevant to any of our theory/experiment comparisons below or to our physical interpretation of any of the results. In contrast, it is useful to compare results with and without continuum solvation, as many calculations in the literature attempt to model solvent via approximations involving a small number of explicit solvent molecules (e.g., a monolayer). This may be adequate for some purposes, but as we show below (e.g., Figure 9), it is inadequate for investigating trapping states associated with adsorbed ions and ambipolar diffusion.

3. RESULTS AND DISCUSSION

3.1. TiO$_2$ Cluster in Continuum Solvent. *3.1.1. Electronic Structure of Neutral and Reduced TiO$_2$ Clusters.* We first optimized the neutral (5,5,5) cluster in continuum water and the converged geometry is shown in Figure 2a. The four sides of the rectangular rutile cluster are (110) surfaces, while the front and back sides are (001) surfaces. Noticeable ripples were generated on the four (110) surfaces and also on the intermediate planes. Only the vertical and horizontal middle (110) planes maintained flatness. Unlike the perfect single crystal, Ti−O bond lengths have a broadened distribution from 1.75 to 2.30 Å, which indicates that surface relaxation makes the cluster more disordered.

The HOMO and LUMO of neutral TiO$_2$ cluster in continuum water are shown in Figure 2b,c. The HOMO is delocalized across the entire cluster along the *c*-axis and is centered entirely on the bridge oxygen atom p-orbitals, which is similar to the valence band in bulk rutile TiO$_2$. The LUMO is delocalized across the vertical middle (110) plane, mainly residing on the titanium d-orbitals which is in agreement with the conduction band in bulk rutile. The electron density of LUMO is concentrated at the three center titanium atoms and gradually decreases when approaching the surface boundary. The HOMO−LUMO gap of the neutral cluster is 3.77 eV in continuum water. This band gap is smaller than our previous result (i.e., 3.91 eV) in the smaller (3,3,3) cluster, which is readily understood from the quantum confinement effects, i.e., when the size of nanoparticle becomes smaller, the band gap correspondingly becomes larger. However, as our model cluster is significantly smaller than the actual TiO$_2$ nanoparticle, the computed band gap is overestimated and larger than the experimental value of 3.0 eV.[53] The overestimation of the band gap compared to experiment can be attributed to a combination of the aforementioned finite size effects and also intrinsic errors in the DFT functional, which are manifested in supercell as well as finite cluster calculations.[68,73]

We then calculated the reduced (5,5,5) cluster by adding one excess electron to the neutral cluster, and the converged geometry is shown in Figure 3a. The equilibrium geometry is very similar to a neutral cluster, and ripples and distortion are
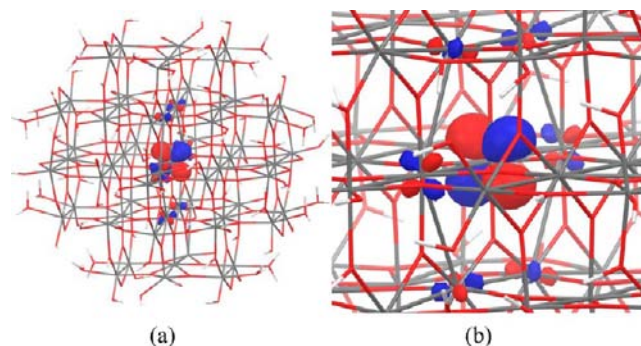

Figure 3. (a) Converged geometry of reduced TiO$_2$ cluster in continuum water, and the MO of excess electron is shown as the red and blue isocontour surfaces. (b) Close view of the MO of excess electron.

also observed in this reduced cluster. The additional electron is delocalized at the center of the cluster shown in Figure 3b, mainly located at the three center titanium d-orbitals. This singly occupied molecular orbital (SOMO) is very similar to the LUMO of the neutral cluster, except that this SOMO is more localized at the center than the LUMO of the neutral cluster and that no electron density of the SOMO resides on the surface titanium atoms. The Franck−Condon relaxation energy due to structural reorganization upon adding one electron to neutral cluster is 0.34 and 0.45 eV in vacuum and in continuum water, respectively.

The electric potential of conduction band was calculated by the definition in Section 2.2 via the half reaction of $[TiO_2] + e^-$ → $[TiO_2(e^-)]$. The computed result (including LOC correction) for (5,5,5) model cluster is −1.02 and −0.20 eV (vs SHE) in vacuum and in continuum water, respectively. The continuum water shifted the conduction band potential to a more positive direction by 0.82 eV when comparing to vacuum.

3.1.2. Finite Size Effect on Solvation Energy of Excess Electron. Clearly, the actual TiO$_2$ nanoparticles in the DSSC, which have a radius of around 20 nm, are substantially larger than our (5,5,5) model cluster. This inappropriate size of our model cluster, due to the compromise between size and computational intensity, leads to the possibility that our model will contain systematic errors when it is used as a model for an actual TiO$_2$ nanoparticle and in predicting physical properties, especially the electric potential we are interested in. To understand the possible origin of the systematic error, we first look at a simplified physical model shown in Figure 4. In the simplest approximation, the TiO$_2$ cluster can be considered as a sphere. In the absence of external cations, such as Li$^+$, the excess electron will be localized in the center of the cluster, as the cluster size increases toward that of an actual TiO$_2$ nanoparticle. In the relatively small clusters we use in the present work, the solvent boundary is close to the excess electron, leading to a significant increase in solvation free energy when the electron is added to the cluster. However, the TiO$_2$ nanoparticles that are actually present in the DSSC have a much larger radius (~20nm), which moves the solvent boundary much further away from the excess electron and thus should substantially diminish the incremental solvation free energy that results from adding the electron. Put simply, there is a finite size effect on the solvation term in our model
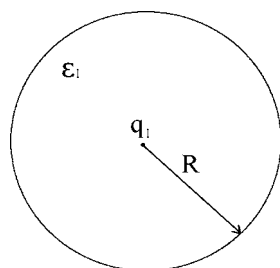
Figure 4. Scheme of a simple model to describe interaction between buried excess electron and continuum solvent; ε is the dielectric constant of the sphere, q is the charge, and R is the radius of the sphere.

calculations which needs to be corrected if we are to profitably compare with experimental data.

We begin by examining the wave function of an excess electron added to our three model clusters, which are displayed in Figure 5 below. It can be seen that the wave functions change its shape and location significantly in each cluster; for example, in the (4,4,4) cluster there is substantial amplitude on six buried Ti atoms and some electron density near the surface of the particle, whereas in the (5,5,5) cluster, the electron density is primarily on a single Ti atom in the center of the cluster and has virtually no density near the surface. The convergence of this wave function with size clearly would benefit from further investigation using larger clusters; we plan to do this in a subsequent publication, relying on increases in computing power, but for the present work, the (5,5,5) cluster was the maximum size we were able to access. In the absence of data from larger clusters, we take the (5,5,5) vacuum energy difference between the neutral and the reduced species to correspond to the value that would be obtained in the actual 20 nm particle; the data from the smaller particles do not enable a reasonable extrapolation to large size, because the excess electron wave functions are so different in character. In support of this approximation, we note that the localization of the wave function in the (5,5,5) particle is substantial and that there is little electron density at or near the surface; it seems likely that this situation will prevail as additional layers are added to the particle. Furthermore, beyond the first few shells of atoms, there are very minimal displacements of Ti or O atoms when the geometry of the cluster is optimized with the excess electron present.
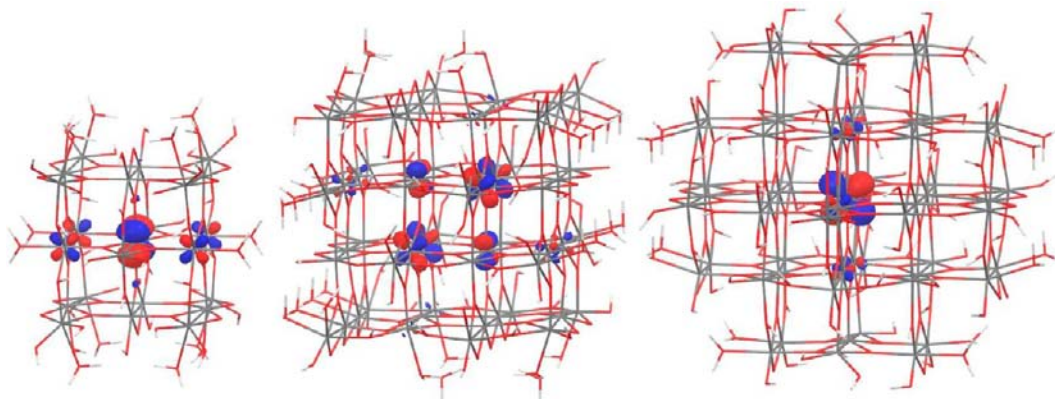
In contrast, there appears to be a significant finite size effect due to solvation for the (5,5,5) particle, which would not be present if the particle were 20 nm in diameter. This is because, as noted above, in a large particle, the solvent boundary would be much further away from the localized electron wave function than it is in the present model system. In a simple Born model, the solvation free energy of a charge embedded in a sphere of radius R which is immersed in solution (with the solvent boundary at R) is proportional to $1/R$. If we plot the solvation free energy of the reduced particle minus that of the neutral particle (the excess solvation free energy due to the injected electron), shown in Figure 6, it can be seen that this quantity is
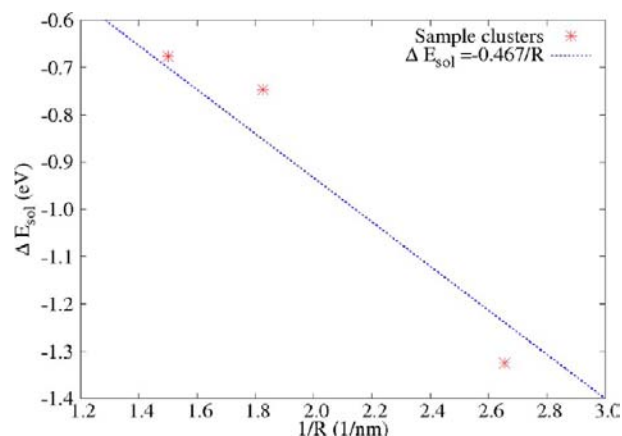

Figure 6. The solvation energy (ΔE_{sol}) contributed by excess electron as a function of the inverse of the averaged cluster radius ($1/R$). The blue dot line shows the linear fitting result, $\Delta E_{sol} = 0.467/R$.

indeed approximately proportional to $1/R$ (the deviations from this dependency are due to the changes in the shape of the electron wave function as well as the fact that the particles are not perfectly spherical), and furthermore that if the value of the solvation free energy is extrapolated to a 20 nm radius, the solvation free energy for that size can be approximated as zero. Therefore, in computing the electric potential in the conduction band, we correct the value obtained from the (5,5,5) model by subtracting the excess solvation free energy as defined above, which is represented by eq 2:

$$E_{excess} = (E_w^A[R] - E_v^A[R]) - (E_w^N[R] - E_v^N[R]) \qquad (2)$$

Figure 5. Location and MO of excess electron in three model clusters with different size (the averaged radii are 0.38, 0.51, and 0.67 nm from left to right). MO is shown as the red and blue isocontour surfaces. The symmetry of cluster used in DFT calculation was D_{2h}, C_{2h}, and C_1 from left to right.

where E is the absolute energy of the cluster, the superscript refers to charged condition of cluster, either neutral (N) or anionic with one excess electron (A), the subscript refers to solvent condition, either in vacuum (v) or in water (w), and R in bracket means the geometry is fixed to be identical to the geometry of the reduced cluster. This correction value for the (5,5,5) cluster is 0.68 eV. We note that in what follows, this finite size correction is applied only in the calculation of the electric potential of the conduction band; in particular it is not applied to surface states, for which we believe the model clusters are physically realistic.

Based on the results above, we are inclined to believe that the excess electron in an actual TiO_2 nanoparticle is very likely to be buried in bulk center and contributes negligible excess solvation free energy. The electric potentials in an actual TiO_2 nanoparticle can be computed as the electric potentials of (5,5,5) cluster with corrected solvation energy, i.e., removing the solvation energy of the excess electron which is due to finite size effects. The electric potentials of conduction and valence bands, obtained after the finite size correction, are −0.88 and +2.89 eV (vs SHE), respectively. The experimentally measured potentials of conduction and valence bands are −0.7 eV and +2.3 eV.[53] Our computed conduction band potential is reasonably in agreement with the experimental result; while the valence band potential is overestimated due to the overestimated band gap discussed above. We assume that the conduction and valence bands do not shift under electron injection and the Li^+ adsorption/intercalation process, and the corresponding electric potentials are constants below.

3.2. TiO$_2$/Li Cluster in Continuum Solvent. In this section, we are focused on the effect of a cation on the electronic trap state in the reduced rutile TiO_2 nanoparticle. The cation we studied is Li^+, which is widely used as the cationic component of the electrolyte of the DSSC. As our ultimate goal is to establish microscopic picture for the ambipolar diffusion process, which requires the simultaneous consideration of solvent, surface, electron, and cation, two kinds of systems were carefully investigated: Li^+ absorbed between bridge oxygens on (110) surface (labeled as O_{Li}), and Li^+ intercalated in the first interstitial shell from TiO_2 cluster (labeled as I_{Li}). Both systems are also of great interest for many experimentalists. The first system is aimed at understanding the effect of Li^+ on the electron trap states, conduction band movement, and in-solvent ambipolar diffusion. The second system is relevant to the questions of how Li intercalation affects the electronic structure of TiO_2 and the effect on electron dynamics. We will answer those questions based on our modeling results and provide a microscopic picture of ambipolar diffusion.

3.2.1. Location of Electron Trap State. The O_{Li} cluster with an excess electron was optimized in vacuum as well as in continuum water, and the converged geometries are shown in Figure 7. The locations of the Li^+ cation are different for vacuum and continuum water cases. In vacuum, Li^+ cation is bonded to two nearest bridge oxygen atoms as well as two surface capping water molecules, which form a square planar structure with Li^+ located at the center. When continuum water is added, the Li^+ cation no longer bonds to the oxygen atoms of surface water molecules, retaining only bonding to the two bridging oxygen atoms and is located on the horizontal middle plane of the cluster. The excess electron is mainly localized at the titanium d-orbital closest to the Li^+ cation for both the vacuum and the continuum water cases.
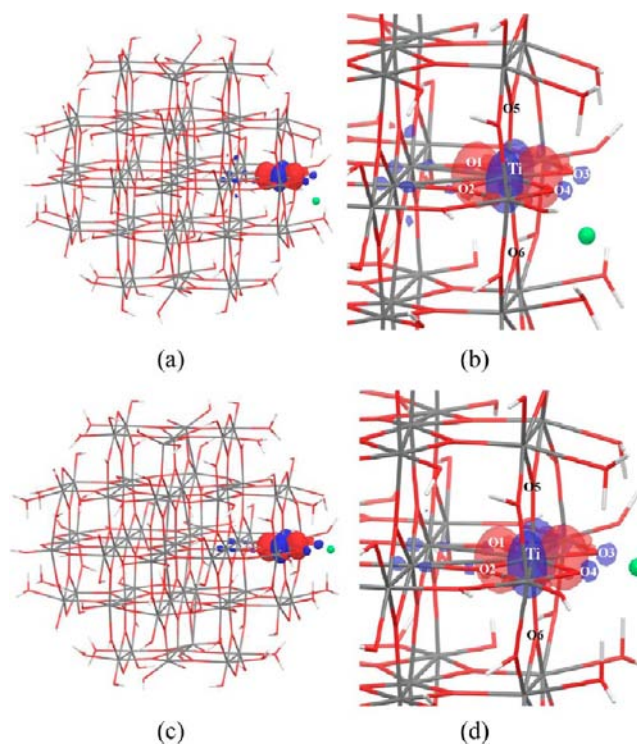

Figure 7. Converged geometry of TiO_2 cluster with surface absorbed Li^+ cation and also an excess electron in vacuum (a,b) and in continuum water (c,d). Titanium, Oxygen, Hydrogen and Lithium atoms are shown in gray, red, white and green, respectively. The MO of excess electron is shown as the red and blue isocontour surfaces. The close views of the MO of excess electron are shown in (b,d). The index definition of six nearest oxygen atoms from Ti^{3+} is given.

In order to discriminate the structure change induced by the Li^+ cation and induced by electron localization, we investigated the bond length changes of the Ti−O bonds around Ti^{3+} in both reduced and unreduced O_{Li} clusters by comparing to the pure neutral TiO_2 cluster, and these results are summarized in Table 2. The results in vacuum and in water are similar, thus we only describe the water case here. When Li^+ is absorbed on the surface via two surface bridging oxygen atoms (labeled as O3 and O4 in Figure 7), the two corresponding bonds Ti−O3 and Ti−O4 are elongated by 0.07 and 0.06 Å, respectively, and on the opposite bulk side, the other two bonds Ti−O1 and Ti−O2 are shortened by around 0.05 and 0.06 Å, which indicate that the adsorption of Li^+ on the surface pushes its nearest Ti atom inside and makes it closer to the bulk region of TiO_2. After the excess electron is localized at the nearest Ti atom, most of Ti−O bonds related to this Ti^{3+} are further elongated, which suggested that the localization of the excess electron weakens the local Ti−O bonding. Next, to further investigate the locality of this structural rearrangement, we studied all Ti−O bond length changes as a function of their distance to Li^+ (graphs are available in the Supporting Information). Most of the large absolute bond length changes occurred within 10 Å from Li^+, which is equivalent to three nearest shells of Ti atoms around Li^+. Outside of three shells, the effect of Li^+ on the Ti−O bond length is negligible.

Similarly, we studied the location of the excess electron and $Li^+/e^−$ induced structural changes, in reduced I_{Li} clusters. The converged cluster and excess electron are shown in Figure 8. The reduced I_{Li} cluster has a similar equilibrium geometry in vacuum and in continuum water except for minor differences

Table 2. Bond Length of Ti^{3+}–O (in Å) for O$_{Li}^{+}$, O$_{Li}$, I$_{Li}^{+}$, and I$_{Li}$ Clusters in Vacuum and in Continuum Water^{a}

cluster	solvent	Ti–O1	Ti–O2	Ti–O3	Ti–O4	Ti–O5	Ti–O6
O$_{Li}^{+}$	vacuum	1.84 (−0.06)	1.87 (−0.09)	2.06 (+0.09)	2.12 (+0.07)	1.86 (−0.03)	2.03 (+0.08)
O$_{Li}$	vacuum	1.99 (+0.09)	2.01 (+0.05)	2.12 (+0.15)	2.13 (+0.08)	1.90 (+0.01)	2.02 (+0.07)
O$_{Li}^{+}$	water	1.86 (−0.05)	1.89 (−0.06)	2.04 (+0.07)	2.09 (+0.06)	1.90 (+0.01)	1.97 (+0.03)
O$_{Li}$	water	2.01 (+0.10)	2.02 (+0.07)	2.11 (+0.14)	2.15 (+0.12)	1.93 (+0.04)	1.97 (+0.03)
I$_{Li}^{+}$	vacuum	1.88 (−0.15)	1.83 (−0.06)	1.93 (−0.13)	2.04 (+0.14)	2.13 (+0.08)	2.04 (+0.15)
I$_{Li}$	vacuum	2.01 (−0.02)	2.00 (+0.12)	1.98 (−0.09)	2.10 (+0.20)	2.12 (+0.07)	2.03 (+0.14)
I$_{Li}^{+}$	water	1.88 (−0.13)	1.83 (−0.06)	1.90 (−0.14)	2.04 (+0.13)	2.15 (+0.12)	2.06 (+0.17)
I$_{Li}$	water	2.01 (−0.01)	2.01 (+0.12)	1.95 (−0.09)	2.11 (+0.20)	2.11 (+0.08)	2.03 (+0.14)

^{a}The bond length changes comparing to pure neutral TiO2 cluster are shown in parentheses. The oxygen indices are defined in Figures 7b,d and 8b.
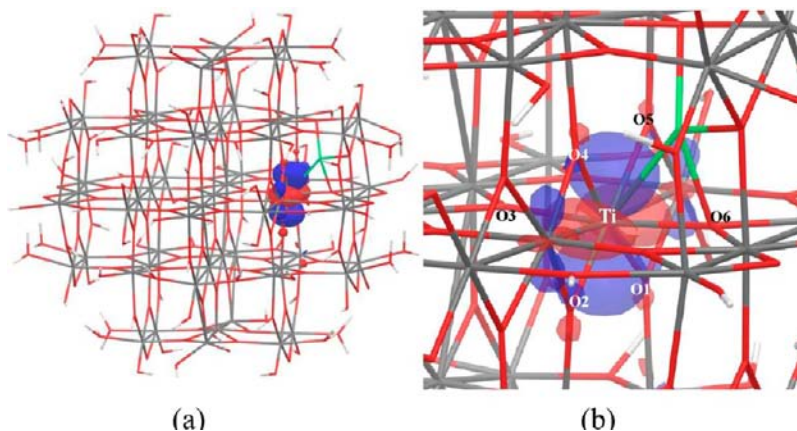

Figure 8. Converged geometry of TiO$_2$ cluster with surface absorbed Li$^+$ cation and an excess electron in continuum water, (vacuum geometry is very similar thus do not show). Titanium, oxygen, hydrogen, and lithium atoms are shown in gray, red, white, and green, respectively. The MO of excess electron is shown as the red and blue isocontour surfaces. The close view of location of excess electron is shown in (b). Index definition of six nearest oxygen atoms from Ti^{3+} is given.

on the surface due to the surface hydrogen-bond network. The Li$^+$ cation is located at the off-center octahedral interstitial site, and the excess electron mainly resides on the nearest Ti atom to Li$^+$ on the bulk side. The bond length analysis, as shown in Table 2, indicates that the insertion of Li$^+$ and the localization of the excess electron induces significant local structural rearrangement in the host cell. The local structural reorganization after the insertion of Li$^+$ is mainly the displacement of the proximate Ti atom away from Li$^+$ and the increase of volume of host cell where Li$^+$ is located. When the extra electron is added, this localized electron on Ti^{3+} significantly elongates the Ti–O bond length of Ti^{3+}. This local structural rearrangement only affects the nearest two Ti shells around Li$^+$.

To summarize, surface-adsorbed and bulk-intercalated Li$^+$ cation traps the excess electron at an electronic state almost completely localized at the nearest Ti d-orbital, forming a conceptual Ti^{3+} site. The addition of Li$^+$/e$^-$ induces significant local structural rearrangement to the local host cell and only affects the nearest three/two Ti shells. The local behavior of the trapped excess electron as well as the local rearrangement of cell are in agreement with the small polaron characteristics of rutile TiO$_2$.

3.2.2. Continuum Solvent Induced Shallow Trap State. We then calculated the trap depth energy for the electron trap state in both O$_{Li}$ and I$_{Li}$ clusters in vacuum as well as in continuum water. The trap depth energy was calculated such that the electric potential of conduction band edge is defined as the zero point, as follows

$$E_{\text{depth}} = \varphi_{\text{trap}} - \varphi_{\text{CB}} \tag{3}$$

where φ_{trap} and φ_{CB} are the electric potentials of the trap state and the conduction band edge, respectively. For φ_{CB} in O$_{Li}$ or I$_{Li}$, we assume that φ_{CB} is equal to that of pure neutral TiO$_2$ cluster and is not affected by adsorption/intercalation of Li$^+$. The φ_{trap} was calculated as the electric potential of O$_{Li}^{+}$ + e$^-$ → O$_{Li}$ and I$_{Li}^{+}$ + e$^-$ → I$_{Li}$. Note that the LOC corrections apply to both trap state and conduction band and have the identical correction value, thus being subtracted out in eq 3; the solvation correction only applies to the conduction band. We summarize the results in Table 3 and Figure 9.

Table 3. Electric Potentials of Conduction and Valence Band Edges and Trap States in Vacuum, in Continuum Water, and in Continuum Acetonitrile

potential (eV, vs SHE)	vacuum	water	acetonitrile
conduction band	−1.02	−0.88	−0.86
O$_{Li}$	+0.07	−0.53	−0.56
I$_{Li}$	+0.31	−0.38	−0.36
valence band	+2.67	+2.89	+2.86

In vacuum, we found the trap depth energies for O$_{Li}$ and I$_{Li}$ clusters were 1.11 and 1.35 eV, respectively, indicating that both trap states are deep traps. Once an electron is trapped by those trap states, it is very difficult for the trapped electron to be thermally activated back to the conduction band. This further implies that these trap states are almost always filled and are not responsible for carrying electric current. However, when the continuum water (or continuum acetonitrile) is added, the electric potentials of both trap states shift to more negative
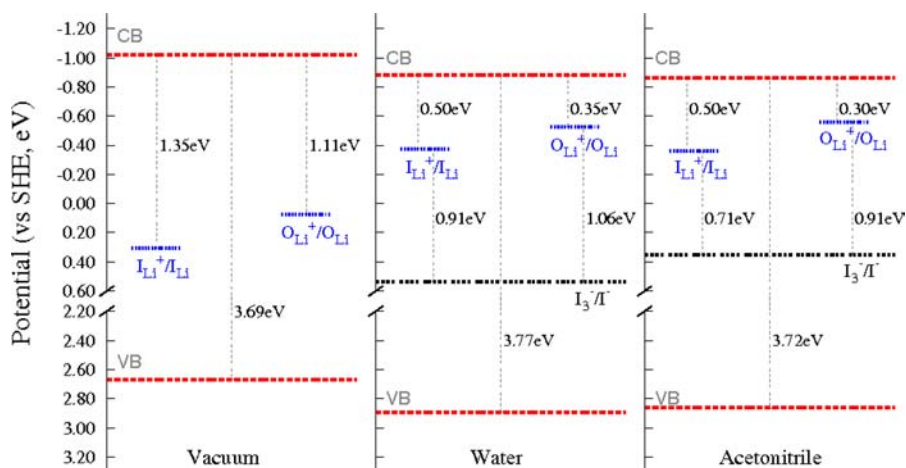
Figure 9. Position of valence and conduction band edges for rutile TiO_2 cluster vs standard hydrogen electrode (SHE) in vacuum, in continuum water, and in continuum acetonitrile. The potentials of the intercalated (I_{Li}^+/I_{Li}) and surface (O_{Li}^+/O_{Li}) trap states and I_3^-/I^- (in water, and in acetonitrile) are shown.

direction by 0.60 and 0.69 eV in water (0.63 and 0.67 eV in acetonitrile) for O_{Li} and I_{Li} clusters, respectively. Counting on this negative shift of trap states as well as the positive shift of conduction band edge, the trap depth energies of O_{Li} and I_{Li} cluster become smaller to 0.35 and 0.50 eV in water (0.30 and 0.50 eV in acetonitrile), which are consistent with experimental value of 0.3−0.5 eV .[54,55,74] We remind the reader that, as discussed previously, "vacuum" here refers to the cluster passivated by a layer of water derived ligands, whereas "water" implies the immersion of this model in a medium of dielectric 80, and "acetonitrile" similarly implies immersion in a medium of dielectric 37.5. Thus the differences in the numbers in Table 3 above reflect the impact of outer shell of solvent. The first layer of water itself will of course shift the results as compared to an unpassivated TiO_2 cluster; thus the shifts presented here should not be misinterpreted as corresponding to that obtained by taking true ultrahigh vacuum derived material and placing it in solution for the first time.

Our results above show that when Li^+ is on surface or in bulk while close to surface boundary, the corresponding electron trap state on the nearest Ti site is a *deep* trap in vacuum but a relatively *shallow* trap in continuum water. The solvation effect of continuum water makes the (near) surface trap state much shallower than it is in vacuum and transforms it from a deep to a shallow trap. The characteristic of existing shallow traps in water differentiates our work on TiO_2/Li system from many prior computational studies on the TiO_2 with oxygen vacancies.[18−20] As the shallow characteristic of trap state originates from solvation effect of continuum solvent, the intercalated Li^+ in deep bulk region, which is far from the surface boundary, should not benefit from the solvation effect and thus creates only the deep trap.

The power law dependence of electron transport on light intensity is often explained by the exponential density of states in TiO_2, however, a model involving two overlapping Gaussian distributions of trap states has also been proposed[56] and is discussed in review articles (e.g., ref 2) as a reasonable alternative to the assumption of an exponential distribution. This charge transport model, developed by Anta and co-workers, can explain the observed power law relation for the kinetics in TiO_2 nanoparticle as well as the exponential model, is based on a combination of two Gaussian distributions of trap states centered at trap energies of about 0.3 and 0.5 eV below

conduction band.[56,57] Our results are almost identical to their reported numbers. As these numbers were arrived at completely independently, and our theoretical numbers were computed from first principles with no adjustment to fit experiment, we consider that the plausibility of the model, involving multiple Gaussian distributions of trap states, has been established.

In fact, there are likely many possible distributions of trap energies which would be compatible with the limited experimental transport data for the Gratzel cell, of which the exponential and multiple Gaussian models are only two examples. Our objective in this paper is not to distinguish between these models, as that is not at all possible based on the limited number of calculations that we have performed, the limitations of our computational modeling, and the challenges posed by the experimental data. Rather, our goal is to establish that the trapping energies that we calculate are compatible with reasonable interpretations of the experimental transport behavior as a function of time and temperature. The comparison made above satisfies this relatively modest, but nontrivial, objective.

3.2.3. Conduction Band Movement. The conduction band movement due to addition of Li^+ cations is an important property which affects the dynamics of electron injection from excited surface dye molecules to the conduction band of the TiO_2 nanoparticle. The influence of the adsorption or intercalation process of Li^+ cation into TiO_2 nanoparticles on conduction band movement is of great interest for experimentalists. These two experimental systems can be modeled by our model clusters: the adsorption case can be mapped to the O_{Li}^+ cluster, representing one Li^+ cation is absorbed on the surface of TiO_2, with no additional electron injected into TiO_2; and the intercalation is modeled by the I_{Li}^+/e^- cluster, which corresponds to the situation in which Li^+ is irreversibly intercalated into TiO_2, and at the same time one electron is trapped nearby to maintain the neutrality of the whole system. Conceptually, no additional electron is injected from surface dyes in our model systems, which is consistent with the dark condition of real measurements. The conduction band movement in these two model clusters was investigated via examining the energetic shift of LUMOs and then comparing them to their counterparts in a pure neutral TiO_2 cluster.

For the O_{Li}^+ cluster, the LUMO is almost identical to the LUMO in the pure neutral TiO_2 cluster. The energetic shift of the LUMO is −38 meV, and the averaged energetic shift of the 50 LUMOs gives −71 ± 8 meV, which is qualitatively in agreement with the experimental result of a −260 meV shift in 0.8 M Li^+ acetonitrile solution,[58] which presumably would cause a larger shift than the single Li^+ cation we use here. Besides, we found the energetic shift of MOs is weakly correlated to their distance to Li^+ cation shown, as in Figure 10, suggesting that Li^+ acts as a screened point charge and the interaction between Li^+ and MOs follows Coulomb's law.
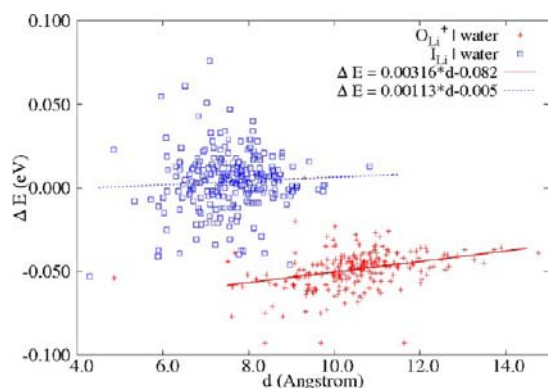

Figure 10. Energy shift of unoccupied molecular orbitals (ΔE) as a function of their distance (d) to Li^+ in O_{Li}^+ (blue) and I_{Li} (red) clusters. The linear fitting for O_{Li}^+ (blue dot line) and I_{Li} (red line) clusters is $\Delta E = 0.00316 \times d - 0.082$ and $\Delta E = 0.00113 \times d - 0.005$, respectively.

For the I_{Li}^+/e^- intercalated case, the LUMO was delocalized Ti d-orbitals on the vertical middle plane, which is the same as the LUMO in the pure neutral TiO_2 cluster. The additional electron was trapped at the Ti atom near Li^+ which is located at the next right-hand-side layer from LUMO. The energetic shift of LUMO is a negligible value of +9 meV, and the averaged energetic shift of 50 LUMOs shown in Figure 10 is 12 ± 13 meV, which is in consistent with the experimental result of approximate zero conduction band movement for Li intercalated TiO_2.[59,60] The computational results suggest that Li^+/e^- pair produces a very limited, if not zero, perturbation on LUMO; the local geometrical reorganization and significant larger standard deviation of energetic shifts indicate that the coupled Li^+/e^- acts more like a small dipole.

3.2.4. Ambipolar Diffusion and Barrier Height. Ambipolar diffusion refers to a process in which an excess electron is transported through a material in concert with small cationic species; the electron is always accompanied by one or more cations, and the cation provides electronic stabilization for the electron throughout its journey from injection to the collection electrode. In the present case, the excess electron is presumed to reside on a single Ti atom (reduced from Ti^{4+} to Ti^{3+}), which in the simplest single cation model (the only one we consider in detail below, due to the restrictions on our computational technology) is stabilized by a Li^+ cation coordinated to the Ti^{3+} ion. The localization of the electron in this mechanism is similar to that which occurs in small polaron self-trapping of an electron in a crystal lattice, with the difference that the some of the energy to drive localization is provided by coordination of an external ion from solution,

along with the usual optimization of bond lengths and angles of coordinating atoms in the lattice that drive polaron formation.

Polaron formation and (possible) migration has been investigated previously in the context of TiO_2, both experimentally and theoretically. Experimental measurements on bulk TiO_2 show a relatively large effective mass for the electron, suggesting some trapping by phonons, but the data are ambiguous with regard to whether a sharply localized small polaron state is the proper description of the species involved in transport, and the situation is further obscured by the possible role of defect states.[69] There are also experiments on TiO_2 particles, one of which detects reduced Ti^{3+} states using EPR experiments.[70] However, these particles contain many defects and impurities, and one can generate the same EPR signal from defect sites without any photoexcitation. Calculations using DFT+U methods (with a large value of U, ~10 eV) show polaron localization,[18,71,72] as do recent B3LYP calculations.[73] The complexity of the experimental systems, and uncertainties in the calculations of various types, makes direct comparison of theory and experiment difficult to achieve in an unambiguous fashion. However, the basic idea that localization on a Ti atom to produce Ti^{3+} is possible provides a useful background for our construction of localized states required for ambipolar diffusion induced by binding of an external cation.

Several different physical processes are possible: A single cation could move with the electron on the entire trajectory, different cations could stabilize the electron at different sites along the trajectory, or a cloud of cations in solution could diffuse with the electron as it hops from site to site. A combination of these processes is also possible. In the present paper, we do not investigate these models in their full generality, as this requires dynamical simulations involving multiple cations which we are at present unprepared to undertake. Rather, we generate illustrative transitions in which the electron is transferred from one acceptor site in the TiO_2 substrate to a neighboring site, and a single cation is closely coupled with the electron. The trajectory of the cation serves as the reaction coordinate, with the electronic structure assumed to adiabatically reorganize as a function of the cation position. From this model, we can extract an activation barrier for a fundamental hopping event and compare the magnitude of this barrier to the distribution of barrier heights estimated by Frank and co-workers from experiments measuring the temperature dependence of electron transport in the DSSC.[2] Our objective here is not to definitively quantitate the transport mechanism but rather to establish the plausibility (via the above comparison with experiment) of the core events in the ambipolar diffusion model. Dynamical simulations involving explicit waters, multiple electrons, and an experimentally realistic cation concentration will be necessary to develop a more detailed picture of the model and its predictions. Such simulations, however, require parametrization of a model of the interaction of the various components; the quantum chemical calculations we report here can be viewed as an essential preliminary step in carrying out such a parametrization.

In the simplified model above, there are three possible Li^+/e^- ambipolar diffusion paths in rutile TiO_2 nanoparticle shown in Figure 11, and we label them as paths A, B, and C. Path A is along the c-axis of rutile TiO_2 in such a way that Li^+ migrates within the c-axis channel, and the localized electron follows Li^+ via hopping between adjacent Ti sites. This path is the most probable ambipolar diffusion path within the cluster, with the lowest activation energy. Path B is similar to path A but is
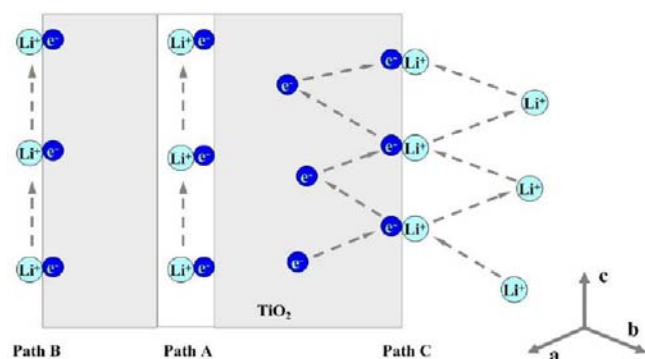
12037

dx.doi.org/10.1021/ja3013787 | *J. Am. Chem. Soc.* 2012, 134, 12028−12042

Figure 11. Scheme of three possible ambipolar diffusion paths in a rutile TiO$_2$ nanoparticle. Path A represents that Li$^+$/e$^-$ migrates along the c channel of rutile TiO$_2$ nanoparticle; path B represents that the Li$^+$/e$^-$ diffuses along the surface via oxygen bridge sites; and path C represents Li+/e$^-$ diffuses via multiple bulk surface hopping processes.

located on the surface of the TiO$_2$ cluster along the *c*-direction oxygen bridge. Path C involves the motion of Li$^+$ toward and away from the TiO$_2$ surface as well as the hopping of the electron between the conduction band edge and the different Li$^+$ induced surface trap states (illustrated in Figure 12). As it is still questionable on how to robustly compute possible finite size correction for transition state (TS) of path C, we leave the calculation of barrier heights of path C for future work.

For path A, ambipolar diffusion within TiO$_2$ along the c channel, we first optimized two ground states (GS) with Li$^+$ located at two adjacent octahedral interstitial sites. As shown in Figure 13 (top), the two GSs are the mirror image of each other except for the disordered surface hydrogen-bond network. Initially, the excess electron is located at the nearest Ti site in the two GSs. The absolute energies of the two GS are very close, and the right GS has a slightly lower energy than the left one, by 0.04 eV. We then calculated the TS for Li$^+$ hopping between the two GS. The Li$^+$ cation finally located at around the middle point of the two adjacent interstitial sites but closer to the left. One would expect that the excess electron is delocalized between two adjacent Ti trapping sites, but this was not observed. Instead, the excess electron is localized at the right Ti trapping site in Figure 13 (top). The barrier heights from the left and right GS to the TS were 0.12 and 0.16 eV, respectively.

For path B, ambipolar diffusion on the surface along *c*-direction oxygen bridge, only one GS was chosen to be

optimized because the other one has a poorly defined geometry, in which the Li$^+$ is located at the boundary and is bonding to an O−H group instead of bridge oxygen. Then the TS of path B was calculated, and the results of GS and TS are shown in Figure 13 (bottom). In the TS, Li$^+$ was located at the middle of two adjacent "conceptual" binding sites. Similar to path A, we did not observe the delocalization of trapped electron, and it is almost completely localized at one Ti site, indicating only small amount of trapped electron density is transferred from the initial to final Ti site at the transition state. The barrier height for path B is 0.25 eV.

Assuming the electron transport in DSSC is coupled with the dynamics of cations in electrolyte (the cations in electrolyte "drag" on the electron transport), our barrier heights from ambipolar diffusion model should be in principle consistent with experimental activation energy (E_a) of electron transport in DSSC. It should be noted that it is likely that many alternative ambipolar diffusion paths can also be constructed which would yield similar transport barriers, so the analysis we provide here represents only establishment of the plausibility of an ambipolar diffusion based model, as opposed to stronger results such as ruling out alternatives. Nevertheless, the results are in satisfactory concordance with experiment: Frank and other groups reported similar E_a values in the range of 0.10−0.27 eV depending on the cell preparation,[61−63] whereas our computed barrier heights are in a similar range of 0.12−0.25 eV. These results validate the consistency of our calculated ambipolar diffusion model with experiment.

Finally, we want to further comment on the physical picture of ambipolar diffusion based on computational results above. As the diffusion of an electron confined on an actual TiO$_2$ nanoparticle is faster than the diffusion of an Li$^+$ cation in electrolyte, the diffusive behavior at short and long time scales should be viewed separately. In a short time scale, which is shorter than the characteristic time of Li$^+$ diffusion, the distribution of Li$^+$ near the surface of TiO$_2$ nanoparticle creates a "static" distribution of shallow trap states, which prevents the fast electron diffusion for the local surface areas. In the long time scale view, the dynamics of Li$^+$ cation in electrolyte creates an averaged distribution of shallow trap states for all Li$^+$ accessible surface areas, these resulting traps slow down the electron diffusion via trapping and detrapping processes.

3.2.5. Open Circuit Voltage and Chemical Reaction Cycle. The open circuit voltage (V_{oc}) in DSSC is the difference between the Fermi level of TiO$_2$ nanoparticles and the redox
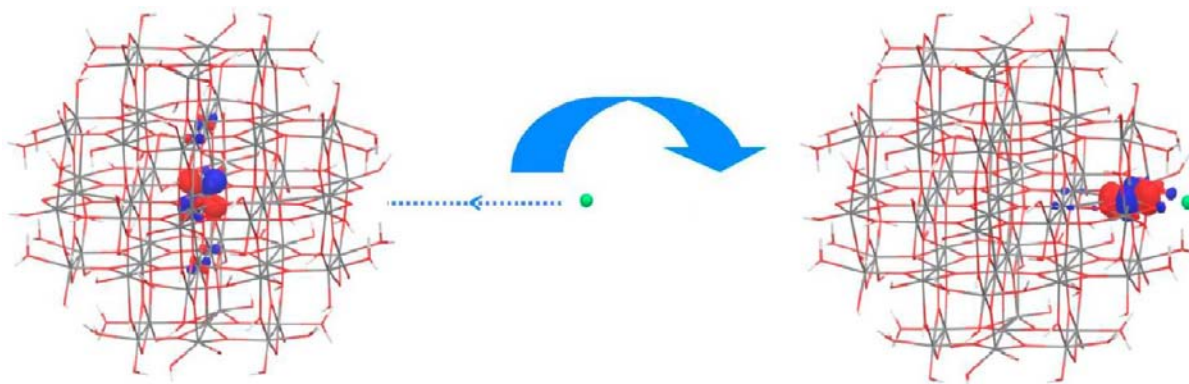

Figure 12. Scheme of the electron hopping from bulk to the surface state due to the motion of Li$^+$ cation in solvent. The hopping electron is shown in red and blue isocontour surfaces, and Li$^+$ is shown in green.
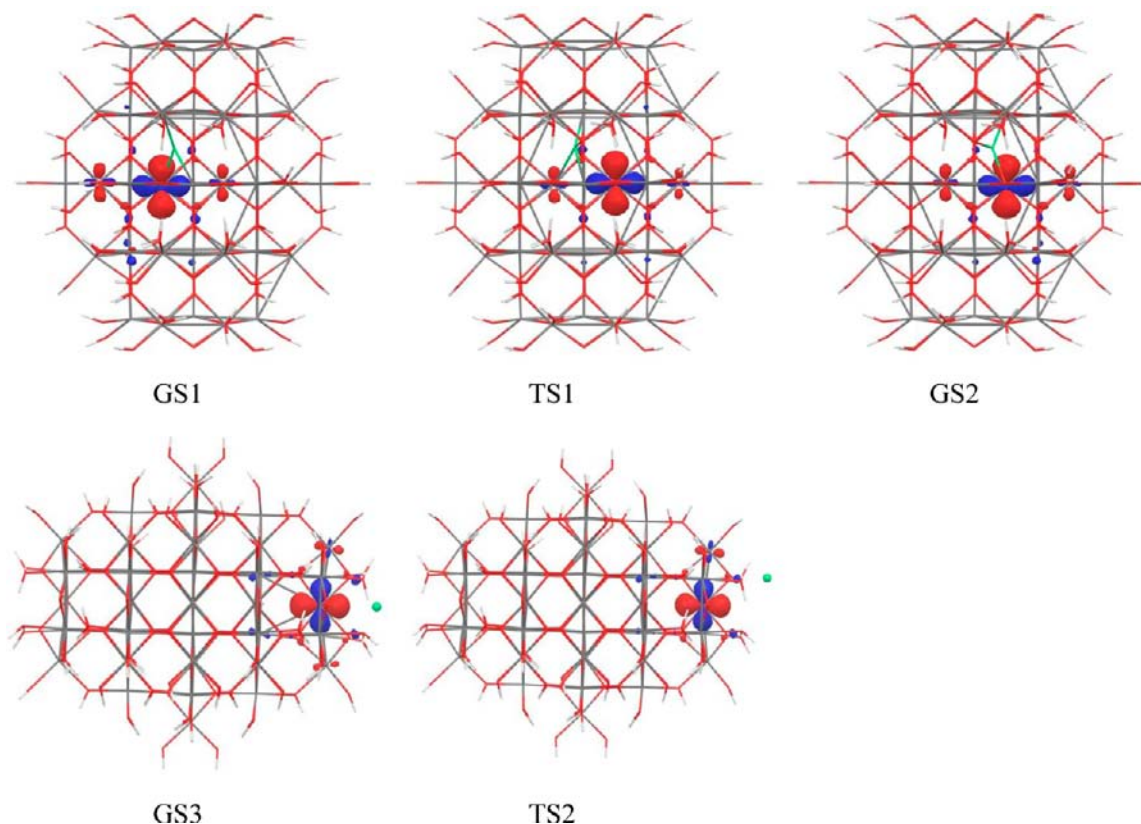
Figure 13. GS and TS for Li$^+$/e$^-$ ambipolar diffusion along paths A (top) and B (bottom). The barrier heights for GS1 → TS1, GS2→ TS1, and GS3 → TS2 are 0.12, 0.16, and 0.25 eV, respectively. The hopping electron is shown in red and blue isocontour surfaces, and Li$^+$ is shown in green.

potential of the electrolyte. The most widely used redox couple in DSSC is I$_3^-$/I$^-$, and the experimental redox potential of I$_3^-$/I$^-$ is +0.54 eV in water[64,65] and +0.35 eV in acetonitrile.[66] The Fermi level of the TiO$_2$ nanoparticle is assumed to be the highest filled energetic level, which is corresponding to the trap states in our model clusters, and hence the V_{oc} can be calculated as the difference of electric potential between trap state and I$_3^-$/I$^-$ redox couple. The values we obtained are 1.06 and 0.91 eV in water (0.91 and 0.71 eV in acetonitrile) for the O$_{Li}$ and I$_{Li}$ model clusters respectively.

We then constructed the possible reaction paths starting from the pure neutral TiO$_2$ cluster and ending at the TiO$_2$/Li complex, as shown in Figure 14, to investigate the chemical equilibrium between TiO$_2$ nanoparticles and Li$^+$. In Figure 14, the left-middle cluster represents the pure neutral TiO$_2$ cluster, which can either bond to Li$^+$ cations in electrolyte via surface adsorption or intercalation process or obtain extra electrons from the surface dye molecules. The formation energies of O$_{Li}^+$ and I$_{Li}^+$ complexes are +2.6 and +9.5 kcal/mol, respectively, indicating that both bonding processes are disfavored in energetics. However, as the formation energy of Li adsorbed complex is just a few kcal/mol larger than zero, if there are *sufficient* Li$^+$ in electrolyte (i.e., the concentration of Li$^+$ is high enough), it is completely possible for some Li$^+$ cations to be adsorbed on the TiO$_2$ surface via oxygen bridges.

After an electron is injected into the TiO$_2$ cluster, a reduced TiO$_2$ cluster is formed, shown in the right-middle of Figure 14. The formation energies for the reduced TiO$_2$ cluster to adsorb or intercalate one Li$^+$ cation are −5.5 kcal/mol and −2.1 kcal/mol for O$_{Li}$ and I$_{Li}$ respectively, indicating that the Li$^+$ cations in the electrolyte are "attracted" by the injected electrons and
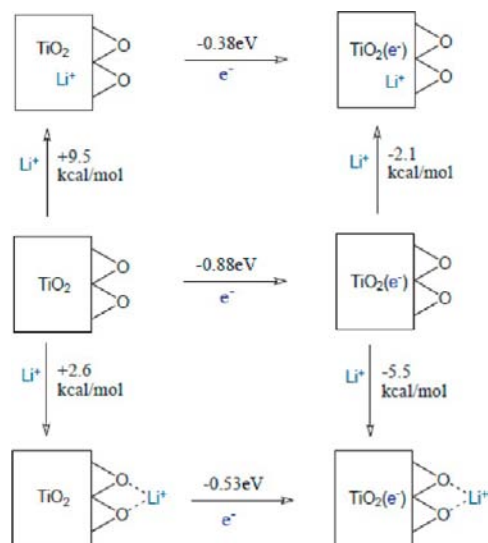

Figure 14. Diagram of chemical cycle.

hence are prefer bonding to the position proximate to where electron is trapped, which is consistent with the picture of ambipolar diffusion discussed above.

If we generalize the physical picture above from our specific model system, containing only one excess electron and one Li$^+$, to the system containing multiple injected electrons and multiple interacting Li$^+$ cations, it is reasonable to believe that multiple Li$^+$/e$^-$ polaron pairs are trapped near the surface and cover certain Li$^+$ accessible surface areas (it is not necessary for this coverage to be a monolayer as the charge−charge repulsion

Table 4. Summary of Predicted Physical Properties and Corresponding Experimental Values

property	DFT (water)	DFT (acetonitrile)	expt.
conduction band edge (eV, vs SHE)	−0.88	−0.86	−0.7[53]
valence band edge (eV, vs SHE)	+2.89	+2.86	+2.3[53]
trap depth (eV)	0.35, 0.50	0.30, 0.50	0.3,[54,a] 0.5,[55,b] 0−0.25[74,c]
band gap (eV)	3.77	3.72	3.0[53]
conduction band movement (meV)			
(a) surface Li$^+$	−71 ± 8	−	−260[58,d]
(b) inserted Li$^+$/e$^-$	12 ± 13	−	∼0[59,60]
diffusion barrier (eV)	0.12−0.25	−	0.10−0.15,[61,e] 0.19−0.27[62,f]
V_{oc} (eV)	0.91[g]	0.71[h]	0.8[1,i]

[a]Rutile TiO_2, 0.1 M [n-Bu$_4$N]ClO$_4$ in acetonitrile, cyclic voltammetry methods. [b]Anatase TiO_2, 0.2 M LiClO$_4$ in water, cyclic voltammetry methods. [c]Rutile TiO_2, proton in water, photoinduced reactions. [d]Rutile TiO_2 with 0.8 mol Li$^+$ in acetonitrile. [e]Anatase TiO_2, 0.5 M LiI in methoxyacetonitrile. [f]Anatase TiO_2, 0.8 M 1,2-dimethyl-3-hexylimidazolium iodide in methoxyacetonitrile. [g]Computed by using the I_3^-/I$^-$ redox potential in water, +0.54 eV (vs SHE). [h]Computed by using the I_3^-/I$^-$ redox potential in acetonitrile, +0.35 eV (vs SHE). [i]AM 1.5 illumination (0.998 suns).

is very strong). In an energetic view, these trapped Li$^+$/polaron pairs form a conceptual surface band which is 0.3−0.5 eV below the conduction band edge of the TiO_2 nanoparticle and allows multiple electron trapping and detrapping processes.

3. Comparison to Experiment Results. We summarize the computational results and corresponding experimental values in Table 4. The DFT calculated electric potential of the conduction band edge (−0.88 eV in water and −0.86 eV in acetonitrile) is close to the experimental measurement of −0.7 eV.[53] The band gap (3.77 eV in water and 3.72 eV in acetonitrile) is overestimated by DFT comparing to the experimental value of 3.0 eV,[53] leading to the more positive valence band potential. The trap depth energies of O_{Li} and I_{Li} clusters from DFT calculations are, in range of 0.30−0.50 eV, consistent with the corresponding experimental measurements.[54,55,74] The conduction band movement predicted by DFT calculations (−71 ± 8 meV) is quantitatively in agreement to the experimental result of −260 meV in 0.8 M Li$^+$ acetonitrile solution, which is presumably larger for a significantly higher Li$^+$ concentration. Finally, the DFT calculated V_{oc} (0.91 eV in water and 0.71 eV in acetonitrile) is close to the experimental measurement of 0.8 eV in the real DSSC.[1]

The agreement between theory and experiment for the wide range of properties that we have reported is uniformly within the range of 0.1−0.2 eV. Given the approximations in constructing the physical model, noise in the experimental data, and possible errors remaining in the DFT, we consider these results to be strongly confirmatory of the fundamental assumptions underlying our approach to modeling the DSSC at an atomic level of detail. The use of a cluster model realistically passivated with water derived ligands, corrections for finite size effects, and employment of a DFT functional, which has been validated in its ability to accurately predict redox potentials for transition-metal-containing systems, have in combination enabled a significant advance in making extensive and quantitative contact with the relevant experimental data. As noted in the Introduction Section, these methods are quite different in aggregate than previous approaches to the problem, and we believe that they provide a path forward to achieving a useful microscopic picture of the functioning not only of the DSSC but also of other nanoscale solar photovoltaic devices. The results also validate the technical improvements that we have made enabling a transition-metal oxide cluster with more than 350 atoms to be studied in the Jaguar electronic structure

program on a routine basis. Without the enhancements in parallelization, initial guess, and convergence of geometry optimization, obtaining numbers that could be compared with experiment, which often involved subtraction of two large values, would not have been possible. The quality of the results compared to experiment demonstrates that the calculations are sufficiently converged (in terms of both geometry and wave function) so that the results are not overwhelmed by random noise fluctuations, a serious danger when treating large systems with many flexible degrees of freedom (here, the passivating water derived ligands).

■ CONCLUSION

We have developed a cluster model of a TiO_2 nanoparticle in the DSSC and used first-principles quantum chemistry, coupled with a continuum solvation model, to compute structures and energetics of key electronic and structural intermediates and transition states. Our results suggest the existence of shallow surface trapping states induced by small cations and continuum solvent effect as well as the possibility of the existence of a surface band which is 0.3−0.5 eV below the conduction band edge. The results are in uniformly good agreement with experiment and establish the plausibility of an ambipolar model of electron diffusion in which small cations, such as Li$^+$, diffuse alongside the current carrying electrons in the device, stabilizing shallowing trapping states, facilitating diffusion from one of these states to another, in a fashion that is essential to the functioning of the cell.

The results of the present paper, coupled with experimental observations of various types, suggest many interesting questions that can be asked in future work. For example, what happens if different cations are used as a component of the electrolyte? Can protons play a similar role to Li$^+$ in an ambipolar diffusion model? What happens if water is completely excluded from the Gratzel cell? The computational platform we have assembled provides an approach to begin to address some of these issues. The more comparisons with experiment that can be made, as features of the cell are varied, the more robustly the quality and predictive power of the modeling can be assessed.

As mentioned above, our intention is to expand the above efforts to perform realistic dynamical simulations of the transport process in the DSSC. We will also investigate in detail the reduction of of the I_3^-/I$^-$ couple, in order to understand the special efficacy demonstrated by this couple in

12040

dx.doi.org/10.1021/ja3013787 | *J. Am. Chem. Soc.* 2012, 134, 12028−12042

functional DSSC applications. With sufficient insights, it will hopefully be possible to design modifications of the current DSSCs which reduce costs, improve reliability, longevity, and environmental suitability (e.g., by replacing the I_3^-/I^- couple by a couple with superior properties in these dimensions). With a solid foundation for the computational methodology, theory can be a suitable partner with experiment in developing such innovations.

■ ASSOCIATED CONTENT

Ⓢ Supporting Information

A detailed description of the methodology of DFT calculations, the figures showing bond length changes as well as the Cartesian coordinates of all clusters are provided. This material is available free of charge via the Internet at http://pubs.acs.org.

■ AUTHOR INFORMATION

Corresponding Author

rich@chem.columbia.edu

Notes

The authors declare the following competing financial interest(s):Richard Friesner has an interest in Schrodinger, Inc. This is fully disclosed in the Acknowledgment section of the manuscript.

■ ACKNOWLEDGMENTS

■ REFERENCES

(1) Grätzel, M. *J. Photochem. Photobiol., C* **2003**, *4*, 145−153.

(2) Frank, A. J.; Kopidakis, N.; Van de Lagemaat, J. *Coord. Chem. Rev.* **2004**, *248*, 1165−1179.

(3) Ardo, S.; Meyer, G. J. *Chem. Soc. Rev.* **2009**, *38*, 115−164.

(4) Grätzel, M. *Acc. Chem. Res.* **2009**, *42*, 1788−1798 PMID: 19715294.

(5) Hagfeldt, A.; Boschloo, G.; Sun, L.; Kloo, L.; Pettersson, H. *Chem. Rev.* **2010**, *110*, 6595−6663.

(6) Peter, L. M. *J. Phys. Chem. Lett.* **2011**, *2*, 1861−1867.

(7) Henderson, M. A. *Surf. Sci. Rep.* **2011**, *66*, 185−297.

(8) Bergström, R.; Lunell, S.; Eriksson, L. A. *Int. J. Quantum Chem.* **1996**, *59*, 427−443.

(9) Albaret, T.; Finocchi, F.; Noguera, C. *J. Chem. Phys.* **2000**, *113*, 2238−2249.

(10) Qu, Z.-W.; Kroes, G.-J. *J. Phys. Chem. B* **2006**, *110*, 8998−9007 PMID:16671707.

(11) Qu, Z.-W.; Kroes, G.-J. *J. Phys. Chem. C* **2007**, *111*, 16808−16817.

(12) Cao, L.-J.; Ai, H.-Q.; Zheng, L.-M.; Wang, S.-N.; Zhou, M.-J.; Liu, J.-F.; Zhang, C. *Int. J. Quantum Chem.* **2011**, *111*, 2416−2427.

(13) Syzgantseva, O. A.; Gonzalez-Navarrete, P.; Calatayud, M.; Bromley, S.; Minot, C. *J. Phys. Chem. C* **2011**, *115*, 15890−15899.

(14) Sahoo, S. K.; Pal, S.; Sarkar, P.; Majumder, C. *Chem. Phys. Lett.* **2011**, *516*, 68−71.

(15) Blagojevic, V.; Chen, Y.-R.; Steigerwald, M.; Brus, L.; Friesner, R. A. *J. Phys. Chem. C* **2009**, *113*, 19806−19811.

(16) Di Valentin, C.; Pacchioni, G.; Selloni, A. *Phys. Rev. Lett.* **2006**, *97*, 166803.

(17) Finazzi, E.; Valentin, C. D.; Pacchioni, G.; Selloni, A. *J. Chem. Phys.* **2008**, *129*, 154113.

(18) Morgan, B. J.; Watson, G. W. *Phys. Rev. B* **2009**, *80*, 233102.

(19) Mattioli, G.; Alippi, P.; Filippone, F.; Caminiti, R.; Amore Bonapasta, A. *J. Phys. Chem. C* **2010**, *114*, 21694−21704.

(20) Deskins, N. A.; Rousseau, R.; Dupuis, M. *J. Phys. Chem. C* **2011**, *115*, 7562−7572.

(21) Ganduglia-Pirovano, M. V.; Hofmann, A.; Sauer, J. *Surf. Sci. Rep.* **2007**, *62*, 219−270.

(22) Pacchioni, G. *J. Chem. Phys.* **2008**, *128*, 182505.

(23) Aiura, Y.; Nishihara, Y.; Haruyama, Y.; Komeda, T.; Kodaira, S.; Sakisaka, Y.; Maruyama, T.; Kato, H. *Phys. B (Amsterdam, Neth.)* **1994**, *194−196* (Part 1), 1215−1216.

(24) Solbrand, A.; Lindström, H.; Rensmo, H.; Hagfeldt, A.; Lindquist, S.-E.; Södergren, S. *J. Phys. Chem. B* **1997**, *101*, 2514−2518.

(25) Van de Lagemaat, J.; Park, N.-G.; Frank, A. J. *J. Phys. Chem. B* **2000**, *104*, 2044−2052.

(26) Kopidakis, N.; Schiff, E. A.; Park, N.-G.; Van de Lagemaat, J.; Frank, A. J. *J. Phys. Chem. B* **2000**, *104*, 3930−3936.

(27) Nistér, D.; Keis, K.; Lindquist, S.-E.; Hagfeldt, A. *Sol. Energy Mater. Sol. Cells* **2002**, *73*, 411−423.

(28) Nakade, S.; Kambe, S.; Kitamura, T.; Wada, Y.; Yanagida, S. *J. Phys. Chem. B* **2001**, *105*, 9150−9152.

(29) Kambe, S.; Nakade, S.; Kitamura, T.; Wada, Y.; Yanagida, S. *J. Phys. Chem. B* **2002**, *106*, 2967−2972.

(30) Koudriachova, M. V.; Harrison, N. M.; de Leeuw, S. W. *Phys. Rev. Lett.* **2001**, *86*, 1275−1278.

(31) Koudriachova, M. V.; Harrison, N. M.; de Leeuw, S. W. *Phys. Rev. B* **2002**, *65*, 235423.

(32) Koudriachova, M. V.; Harrison, N. M.; de Leeuw, S. W. *Solid State Ionics* **2003**, *157*, 35−38.

(33) Koudriachova, M. V.; Harrison, N. M.; de Leeuw, S. W. *Solid State Ionics* **2004**, *175*, 829−834.

(34) Kerisit, S.; Rosso, K. M.; Yang, Z.; Liu, J. *J. Phys. Chem. C* **2009**, *113*, 20998−21007.

(35) Sushko, M. L.; Rosso, K. M.; Liu, J. *J. Phys. Chem. Lett.* **2010**, *1*, 1967−1972.

(36) Sushko, M. L.; Rosso, K. M.; Liu, J. *J. Phys. Chem. C* **2010**, *114*, 20277−20283.

(37) Zukalová, M.; Kalbác, M.; Kavan, L.; Exnar, I.; Graetzel, M. *Chem. Mater.* **2005**, *17*, 1248−1255.

(38) Panduwinata, D.; Gale, J. D. *J. Mater. Chem.* **2009**, *19*, 3931−3940.

(39) Arrouvel, C.; Parker, S. C.; Islam, M. S. *Chem. Mater.* **2009**, *21*, 4778−4783.

(40) Hughes, T. F.; Friesner, R. A. *J. Chem. Theory Comput.* **2012**, *8*, 442−459.

(41) Hughes, T. F.; Friesner, R. A. *J. Chem. Theory Comput.* **2011**, *7*, 19−32.

(42) *Jaguar*, version 7.7; Schrödinger, LLC: New York, 2010.

(43) Morris, D. Ionic radii and enthalpies of hydration of ions. In *Structure and Bonding (Berlin)*; Springer: Berlin/Heidelberg, Germany, 1968; Vol. 4, pp 63−82; 10.1007/BFb0119185.

(44) Conway, B. E. *J. Solution Chem.* **1978**, *7*, 721−770, DOI: 10.1007/BF00643580.

(45) Marcus, Y. *J. Chem. Soc., Faraday Trans.* **1991**, *87*, 2995−2999.

(46) Schmid, R.; Miah, A. M.; Sapunov, V. N. *Phys. Chem. Chem. Phys.* **2000**, *2*, 97−102.

(47) Friesner, R. A.; Knoll, E. H.; Cao, Y. *J. Chem. Phys.* **2006**, *125*, 124107.

(48) Knoll, E. H.; Friesner, R. A. *J. Phys. Chem. B* **2006**, *110*, 18787−18802.

(49) Goldfeld, D. A.; Bochevarov, A. D.; Friesner, R. A. *J. Chem. Phys.* **2008**, *129*, 214105.

(50) Hall, M. L.; Goldfeld, D. A.; Bochevarov, A. D.; Friesner, R. A. *J. Chem. Theory Comput.* **2009**, *5*, 2996−3009.

(51) Hall, M. L.; Zhang, J.; Bochevarov, A. D.; Friesner, R. A. *J. Chem. Theory Comput.* **2010**, *6*, 3647−3663.

(52) Klamt, A.; Schuurmann, G. *J. Chem. Soc., Perkin Trans. 2* **1993**, 799−805.

(53) Kruczynski, L.; Gesser, H. D.; Turner, C. W.; Speers, E. A. *Nature* **1981**, *291*, 399−401.

(54) Lin, M.-S.; Hung, N.; Wrighton, M. S. *J. Electroanal. Chem. Interfacial Electrochem.* **1982**, *135*, 121−143.

(55) Boschloo, G.; Fitzmaurice, D. *J. Phys. Chem. B* **1999**, *103*, 2228−2231.

(56) Anta, J. A.; Nelson, J.; Quirke, N. *Phys. Rev. B* **2002**, *65*, 125324.

(57) Bisquert, J. *Phys. Chem. Chem. Phys.* **2008**, *10*, 3175−3194.

(58) Park, N.-G.; Chang, S. H.; Van de Lagemaat, J.; Kim, K.-J.; Frank, A. J. *Bull. Korean Chem. Soc.* **2000**, *21*, 985−988.

(59) Meekins, B. H.; Kamat, P. V. *ACS Nano* **2009**, *3*, 3437−3446 PMID: 19873988.

(60) Kopidakis, N.; Benkstein, K. D.; Van de Lagemaat, J.; Frank, A. J. *J. Phys. Chem. B* **2003**, *107*, 11307−11315.

(61) Boschloo, G.; Hagfeldt, A. *J. Phys. Chem. B* **2005**, *109*, 12093−12098.

(62) Kopidakis, N.; Benkstein, K. D.; Van de Lagemaat, J.; Frank, A. J.; Yuan, Q.; Schiff, E. A. *Phys. Rev. B* **2006**, *73*, 045326.

(63) Greijer Agrell, H.; Boschloo, G.; Hagfeldt, A. *J. Phys. Chem. B* **2004**, *108*, 12388−12396.

(64) Stanbury, D. M. *Reduction Potentials Involving Inorganic Free Radicals in Aqueous Solution*; Academic Press: Waltham, Massachusetts, 1989; Vol. *33*, pp 69−138.

(65) Boschloo, G.; Hagfeldt, A. *Acc. Chem. Res.* **2009**, *42*, 1819−1826 PMID:19845388..

(66) Datta, J.; Bhattacharya, A.; Kundu, K. K. *Bull. Chem. Soc. Jpn.* **1988**, *61*, 1735−1742.

(67) Baik, M.-H.; Friesner, R. A. *J. Phys. Chem. A* **2002**, *106*, 7407−7412.

(68) Labat, F.; Baranek, P.; Domain, C.; Adamo, C. *J. Chem. Phys.* **2007**, *126*, 154703.

(69) Yagi, E.; Hasiguti, R. R.; Aono, M. *Phys. Rev. B* **1996**, *54*, 7945.

(70) Berger, T.; Sterrer, M.; Sterrer, M.; Knözinger, E.; Panayotov, D.; Thompson, T. L.; Thompson, T. L. *J. Phys. Chem. B* **2005**, *109*, 6061−6068.

(71) Deskins, N. A.; Dupuis, M. *Phys. Rev. B* **2007**, *75*, 195212.

(72) Deskins, N. A.; Dupuis, M. *J. Phys. Chem. C* **2009**, *113*, 346−358.

(73) Valentin, C. D.; Selloni, A. *J. Phys. Chem. Lett.* **2011**, *2*, 2223−2228.

(74) Ikeda, S.; Sugiyama, N.; Murakami, S.; Kominami, H.; Kera, Y.; Noguchi, H.; Uosaki, K.; Torimoto, T.; Ohtani, B. *Phys. Chem. Chem. Phys.* **2003**, *5*, 778−783.

(75) Hughes, T. F.; Harvey, J. N.; Friesner, R. A. *Phys. Chem. Chem. Phys.* **2012**, *14*, 7724.